Computers & Geosciences 38 (2012) 62–67

Contents lists available at ScienceDirect

Computers & Geosciences

journal homepage: www.elsevier.com/locate/cageo

Interpreting temperature–strain data from mesoscale clathrate experiments

J.R. Leeman [a,b], C.J. Rawn [c], S. Ulrich [b], M. Elwood Madden [a,b], T.J. Phelps [b,*]

[a] School of Geology and Geophysics, University of Oklahoma, 100 E. Boyd, Norman, OK 73019, United States
[b] Biosciences Division, Oak Ridge National Laboratory, Oak Ridge, TN 37831, United States
[c] Materials Science and Technology Division, Oak Ridge National Laboratory, Oak Ridge, TN 37831, United States

ARTICLE INFO

Article history:
Received 18 August 2010
Received in revised form
9 March 2011
Accepted 1 May 2011
Available online 21 June 2011

Keywords:
Fiber Bragg gratings
Gas hydrate
Seafloor stability
Temperature–strain data
Distributed sensing

ABSTRACT

Gas hydrates may play an important role in global climate change, carbon sequestration, energy production and seafloor stability. However, formation and dissociation pathways in geologically complex systems are poorly defined. We present a new approach to processing large amounts of data from a LUNA distributed sensing system (DSS) in the seafloor process simulator (SPS) at Oak Ridge National Laboratory to monitor and visualize gas hydrate formation and dissociation in heterogeneous sediments. The DSS measures relative temperature/strain change with a high spatial resolution allowing the heat of reaction during gas hydrate formation/dissociation to be used to locate clathrate processes in space and time within the vessel. Optical fibers are placed in the sediment following an Archimedean spiral design and the position of each sensor is determined iteratively over the arc length using Newton's method. The DSS data are then gridded with a natural neighbor interpolation algorithm to allow contouring. The locations of sensors on the fiber were verified with hot and cold stimuli in known locations. Software was developed to produce temperature/strain linear and polar plots, which aid in locating significant hydrate formation/dissociation events. Results from an experiment using a vertically split column of sand and silt clearly showed initial hydrate formation in the sand, followed by slow encroachment into the silt. Similar systems and data processing techniques could be used for monitoring of hydrates in natural environments or in any situation where a hybrid temperature/strain index is useful.

1. Introduction

Gas hydrates, a type of clathrates, are cagelike structures of water molecules bonded to form cavities, which are populated by gas molecules such as carbon dioxide or methane. Natural gas hydrates are stable at low temperatures and moderate pressures, making the seafloor an ideal environment for methane hydrate formation. Gas hydrates are sensitive to changes in pressure and temperature; dissociation can be triggered by lowering the water column or by increasing temperature (Buffet and Archer, 2004; Makogon et al., 2007; Sloan, 1998). Hydrates are also subject to action by chemical inhibitors, which increase the required pressure and decrease the temperature conditions for clathrate stability.

Gas hydrates have been proposed as a sequestration mechanism for carbon dioxide (Brewer et al., 2000; Gabitto and Tsouris, 2006; Goel, 2006; Jadhawar et al., 2006) and hydrates of natural gases could provide significant volumes of methane for energy production (Boswell, 2007; Moridis et al., 2009; Walsh et al., 2009). Gas hydrates could also be used as a transport or storage mechanism for gases under low temperature and moderate pressure conditions (Chatti et al., 2005). In addition, dissociation of gas hydrates may have contributed to past global warming events (Kennett et al., 2000; Beauchamp, 2004; Dickens et al., 1997; Maclennan and Jones, 2006; Max et al., 1999; Padden et al., 2001; Weissert and Erba, 2004). Dissociation of hydrates present in seafloor sediments could also result in seafloor instability (Mienert et al., 2005; Kvenvolden, 1999). However, current estimates of hydrate volume vary by many orders of magnitude (Klauda and Sandler, 2005) and constraining these values would be of great aid in determining both the role of gas hydrates in global climate change and the feasibility of producing natural gas from hydrate reservoirs. Therefore, experiments examining and visualizing the formation and dissociation pathways of gas hydrates within sediments have an impact on the assessment of both geological and industrial hazards.

High-resolution data collected through long experiments and effective visualization methods are required to understand the complex behavior of a sediment–hydrate system. Previous workers have used X-ray (Kneafsey et al., 2007) and acoustical (Waite et al., 2004) tomography, neutron diffraction (Thompson et al., 2006), and magnetic resonance imaging (Gao et al., 2005) to observe hydrate formation and dissociation in situ. Fiber optic sensing can also be utilized for effective visualization of hydrate

* Corresponding author.
E-mail address: phelpstj@ornl.gov (T.J. Phelps).

0098-3004/$ - see front matter © 2011 Elsevier Ltd. All rights reserved.
doi:10.1016/j.cageo.2011.05.004

formation within sediment. This paper focuses on data processing methods developed to analyze and visualize large data sets collected by a fiber optic distributed sensing systems (DSS) within complex, multicomponent hydrate experiments in the Seafloor Process Simulator (SPS) at ORNL (Phelps et al., 2001; Rawn et al., 2011).

2. Materials and methods

Mesoscale laboratory experiments help bridge the gap between expensive and difficult field-based analysis of natural hydrates in situ or within preserved cores, and microscopic or molecular-scale measurements of synthetic hydrates, which lack sufficient scale to realize the complexity of natural systems. The SPS is a 72-L pressure vessel 0.33 m in diameter and 0.9 m in length. Designed and constructed at Oak Ridge National Laboratory, the SPS is capable of maintaining pressures up to 20 MPa between 271 and 288 K (Fig. 1) (Phelps et al., 2001). The SPS is made of Hastelloy, a corrosion-resistant nickel-rich steel alloy, and is equipped with 41 pass-through ports for instrumentation, visualization (sapphire windows), or fluid delivery. The vessel is protected from overpressurization by a burst disk. A cold room equipped with an explosion-proof gas evacuation system and monitoring equipment houses the SPS during experiments.

To investigate the effect of sediment size on hydrate formation pathways, a column of sediment split vertically with fine mesh to divide Ottowa sand (500 μm) from silt (67 μm) was placed within the SPS for hydrate formation experiments (C in Fig. 1).

To maintain thermal and pressure equilibrium between the heterogeneous sediment system and the gas to be injected, a second, much smaller, 12-L pressure vessel (0.69-MPa pressure rating) containing the hydrate-forming gas (B in Fig. 1) sits on top of a 20-L sediment column within the SPS. A high-performance liquid chromatography (HPLC) pump injects a water mixture containing 2% methanol to displace gas from the secondary vessel through a branched diffuser (pressure is applied to both outlets, sand and silt) and raise the pressure of the SPS (Fig. 1). Methanol is a hydrate inhibitor and thus prevents hydrate formation inside the secondary vessel. The gas from the secondary vessel is forced through a diffuser into the lower portion of the sediment column to simulate natural gas flow in seafloor sediments. Gas is delivered simultaneously to both the sand and silt sides of the column through screened outlets connected with a '*T*' fitting.

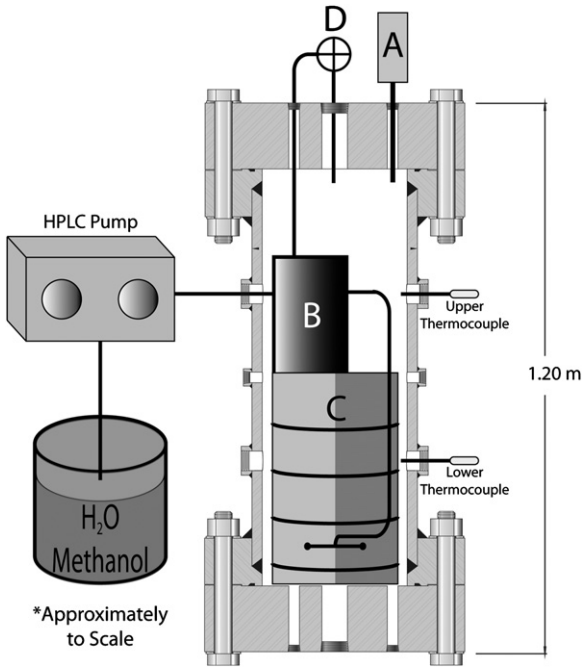

Fig. 1. Configuration of the Seafloor Process Simulator. Two Hastelloy-cased type K thermocouples (both in free gas) and a pressure transducer (A) are used in addition to the DSS system to monitor hydrate formation and dissociation. The 12-L internal pressure vessel (B) rests on top of the sediment column to allow methane gas to equilibrate with the vessel conditions prior to injection. DSS grids are placed at 5, 15, 25, and 35 cm from the bottom of the sediment, represented as black lines in the sediment column (C). The dots at 10 cm indicate the location of the diffuser screens, which were connected via a '*T*' fitting. The sediment column is vertically split with a fine mesh between sand and silt. An equilibrium control value (D) is situated outside the vessel for easy access.

The vessel is monitored by multiple systems that record the pressure and temperature in the headspace and temperature–strain values from the DSS in the sediment throughout the experiment. Gas hydrate formation is an exothermic reaction and dissociation is endothermic. Assuming the vessel and sediment are in thermal equilibrium prior to injection, increasing temperatures within the sediment indicate areas where clathrate is likely forming and lower temperature values indicate that hydrate is likely decomposing. A LabView interface monitors the pressure and temperature of the vessel and the temperature of the cold room to determine external controls on the thermal state of the system. A LUNA Innovations distributed sensing system (DSS) monitors the temperature–strain value along fiber optic cables, which are embedded within the sediment column prior to the experiments. The fibers, coated with Teflon to help reduce the strain response in the measurements and increase their durability, are tied to a plastic mesh along a path approximated by an Archimedean spiral to provide a suitable mechanism for mathematical modeling and then embedded in the sediment. See Rawn et al. (2011) for further details on the operation of the DSS within the vessel.

The DSS measures hybrid temperature–strain values at discrete locations along the fiber optic cable. Bragg gratings are embedded at 1-cm intervals along each fiber utilized by the DSS. The optical properties of the gratings change with temperature and strain due to changes in the grating size, therefore changing the Bragg wavelength (Hill and Meltz, 1997). By sensing changes in the properties of the Bragg gratings, the DSS determines temperature–strain changes at each point.

The DSS relies upon optical principles described by Jones calculus. As light of some arbitrary initial polarization passes through an optical device, its properties change predictably. Polarization of the light can be described with a Jones vector, and the optical device it passes through can be represented by a 2×2 Jones matrix (Jones, 1941). Approximately 100–250 gratings per fiber are read individually along each fiber 1–2.5 m long by an optical backscatter reflectometer (OBR) as it sweeps through a range of wavelengths. The returned wavelength is then interpreted as a hybrid temperature–strain value (TSV), resolving changes as small as 1 μstrain (dimensionless strain quantity, e.g., 10^{-6} m/m) or 0.1 K.

Each DSS fiber was calibrated to correct for birefringence (double refraction) and other optical effects that result from asymmetries in the fiber prior to the experiment. During and following gas injection, data are recorded from each grating in a delimited text file every minute. The system collects approximately 96,240 data points per hour, so the average week-long experiment produces approximately 16 million data points.

The *P–T* data system produces a modest number of data in comparison to the DSS. The bulk vessel pressure is recorded to a precision of 68.9 Pa (0.1 psi), and temperature is monitored at two locations (upper and lower positions) in the vessel with a resolution of 0.1 K every minute.

Using these varied monitoring systems, the hydrate formation and dissociation process is well documented (Rawn et al., 2011; Ulrich et al., 2008). However, integrating results from the separate systems makes interpretation of results difficult, particularly mapping and quantifying significant formation and dissociation events. Bulk temperature and pressure data collected by thermocouples and pressure transducers in the headspace of the SPS provide time series data at one location within the vessel. The DSS provides hundreds of measurements per fiber per time step, creating data files that are challenging to analyze and display due to their size and multidimensional nature.

3. Data processing

The large volume of data produced with the DSS is difficult to process and display in a fashion that allows the full experiment to be visualized in 4-D without shadowing any data. Three-dimensional data plots for an individual fiber can be constructed with graphing software. These plots display the time steps on the x-axis, TSV on the z-axis, and sensor number on the y-axis (Ulrich et al., 2008). Though all the data points are plotted in these figures, some are shadowed by other data in the TSV record (Fig. 2). In addition, it is difficult to determine the location of a given sensor in the vessel in this format; the visualization shows the fiber as if the collection of points were in a straight line, rather than spirals stacked within the column.

3.1. Temperature–strain value animation

Instead of visualizing all the data in one plot as attempted previously (Ulrich et al., 2008), this work aims to produce sequential time series plots of TSV data. To compare TSV data collected on multiple fibers during a single time step, software was written using the open source language Python and the Matplotlib module to produce an individual graph at each time step of the hybrid-TSV value vs sensor position on the fiber. This allows analysis of TSV values over the entire length of multiple fibers at an instant in time, an example of which is shown in Fig. 3. Graphs for each time step throughout the experiment were then animated into movie form. The data were smoothed with a moving average of k points on either side of the current time t at sensor n to help reduce spurious peaks when necessary using the

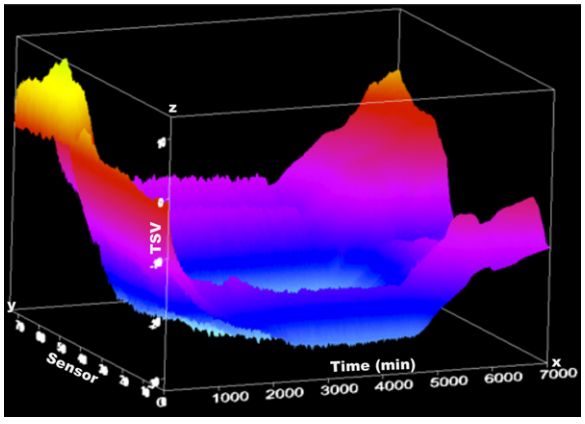

Fig. 2. Three-dimensional plots of TSV data with time on x-axis, sensor number on y-axis, and TSV value on z-axis. Some data are shadowed or hidden by other data points. Wall effects are also visible as fiber(s) leave sediments. Coloring is directly tied to z-coordinate. Modified from Ulrich et al., 2008. (For interpretation of the references to color in this figure legend, the reader is referred to the web version of this article.)

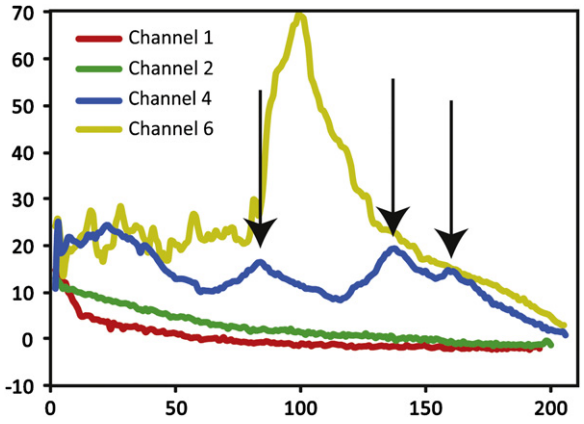

Fig. 3. TSV graph. Each DSS fiber is represented by one line. Three maxima on channel 4 indicate hydrate formation on one side of the sensor plane, cutting across three turns of the spiral.

equation

$$\mathrm{TSV}_{\mathrm{avg}}(n,t)=\frac{\sum_{i=t-k}^{t+k}\mathrm{TSV}(n,i)}{2k+1}. \quad (1)$$

Though this format was helpful to visualize all the data with no shadowing, locating hydrate formation and dissociation periods required identifying areas of rapid TSV change. For this purpose a similar sequence of graphs was constructed with sensor number on the x-axis and ΔTSV or an offset moving average of ΔTSV,

$$\Delta\mathrm{TSV}_{\mathrm{avg}}(n,t)=\mathrm{TSV}_{\mathrm{avg}}(n,k,t+1)-\mathrm{TSV}_{\mathrm{avg}}(n,k,t), \quad (2)$$

on the y-axis. This is done by taking the difference of two time offset moving averages to produce a ΔTSV animation. ΔTSV animations were then used to identify areas of interest.

3.2. Spiral geometry

To fully visualize the geometry of hydrate formation within the sediment column, plotting the location of sensors on each plane in 2-D space is essential. The third, vertical, dimension within the sediment is known and constant for all sensors in a given plane. Plotting the position of the sensors allows figures to be produced that show the position of hot and cold regions in the column of sediment to determine likely locations of gas hydrate formation and dissociation.

The Archimedean spiral of each fiber optic cable is described by the equation

$$r=a+b\theta^{1/c}. \quad (3)$$

The parameter a rotates the spiral, b determines the spacing between the turns,

$$b=\frac{h}{2\pi}, \quad (4)$$

and c determines the spiral type and is equal to 1 for the normal Archimedean geometry. Thus spiral radius (r) grows by a constant amount (h) per turn (2π).

The arc length (s) of the spiral can therefore be described as

$$s=\int_{\theta_1}^{\theta_2}\sqrt{r^2+\left(\frac{dr}{d\theta}\right)^2}\,d\theta \quad (5)$$

with radius r and angle θ. A first central difference approximation,

$$f'\approx\frac{f(x+h)-f(x-h)}{2h}, \quad (6)$$

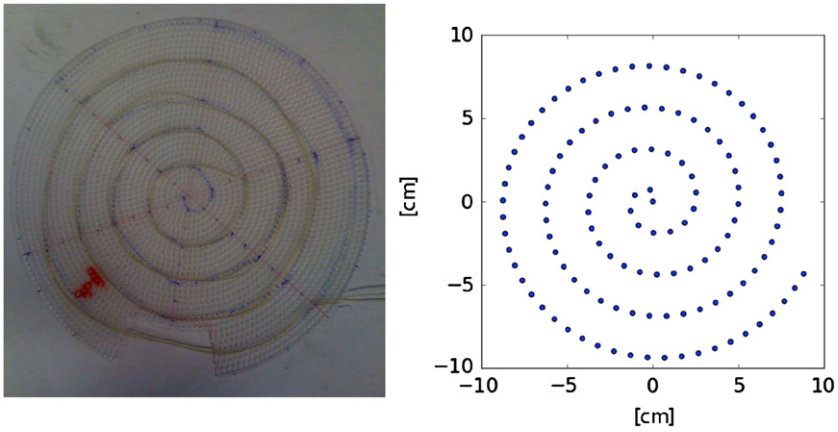

Fig. 4. Physical fiber (left) and mathematical model (right) appear to be good matches, allowing data to be gridded from the model for further interpolation and interpretation.

can be used for programmatic evaluation of the derivative or an absolute difference in the values of dr and $d\theta$.

There is no analytic solution to Eq. (5); therefore, Newton's method is employed as a numerical technique,

$$x_{n+1} = x_n - \frac{f(x_n)}{f'(x_n)}, \tag{7}$$

where x_{n+1} and x_n represent the next and current estimates of the root in question for the function $f(x)$.

Newton's method converges quickly when the initial guess is the location of the last known sensor. If this method of guess selection fails after 20 iterations, the software attempts a bisection method (though this has not occurred in data analysis to this time, it is included in the code for completeness). Numerical convergence could be achieved faster if an analytical function were provided for the derivative. We chose to use numerical derivatives to increase the flexibility of the code and allow any function to be used when describing the fiber geometry. When the output of the spiral model is compared visually with the fiber, it appears to be a good approximation of the physical spiral (Fig. 4).

3.3. Gridding and contouring temperature–strain value data

With the location of the Bragg gratings known, the TSV values can be gridded to allow contouring of the data. Gridding is accomplished with natural neighbor interpolation based on the Delaunay triangulation in the Matplotlib Python package. The basic form of natural neighbor interpolation is given in the equation

$$G(x,y) = \sum_{i=1}^{n} w_i f(x_i,y_i), \tag{8}$$

where w_i are weights, $f(x_i,y_i)$ is known data at (x_i,y_i) and $G(x,y)$ is the estimate at (x,y).

This griding function (called griddata in Python) is generally stable, except for extreme cases, in which it utilizes a toolkit based on National Center for Atmospheric Research (NCAR) gridding software (Sibson, 1981). (Not required for our data.) Abramov and McEwen (2004) evaluated several different interpolation algorithms for laser altimeter data and found the natural neighbor algorithm to be adequate for data sets larger and more sparsely populated than those considered here. Hot and cold areas in initial tests are well resolved with natural neighbor interpolation (Fig. 5); however, further study of different gridding algorithms could lead to improvements in this process.

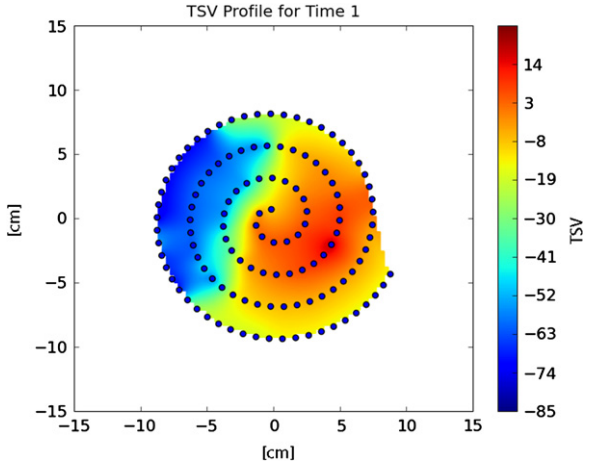

Fig. 5. Results from hot/cold tests on a spiraled DSS fiber. Color is a proxy for the combined TSV on the fiber. (For interpretation of the references to color in this figure legend, the reader is referred to the web version of this article.)

4. Data analysis

Data analysis begins by producing all relevant visualization tools, or products: graphs of headspace P–T data with time through the experiment and graphs of DSS data from the sediment column. ΔTSV data are used to identify time periods and fiber locations of interest. The TSV and P–T products are then inspected, with special attention given to the areas identified in the ΔTSV animations (Fig. 6). This results in a more efficient analysis, likely drawing more conclusions than one could without the synchronous use of multiple data products. For example, subtle changes in the data were identified using this ensemble approach that had been overlooked when the data sets were examined individually. The DSS ΔTSV products highlight areas of potential interest, which trigger closer inspection of small changes in pressure and temperature in the bulk LabView P–T data. This provides multiple data sets, which may confirm hydrate formation/dissocation and constrain the location and extent of hydrate involved.

Data visualization was further extended by rotating each polar plot (representing a single optical fiber) and stacking them for easy comparison of hydrate formation/dissociation processes along planes at different levels within the vessel (Fig. 7). Hydrate formation between the planes must be inferred through interpolation using Eq. (8), since sensors are not present in the gap. Simple natural neighbor interpolation yields insight into the possible structure of hydrate within the sediment. The linear nature of the

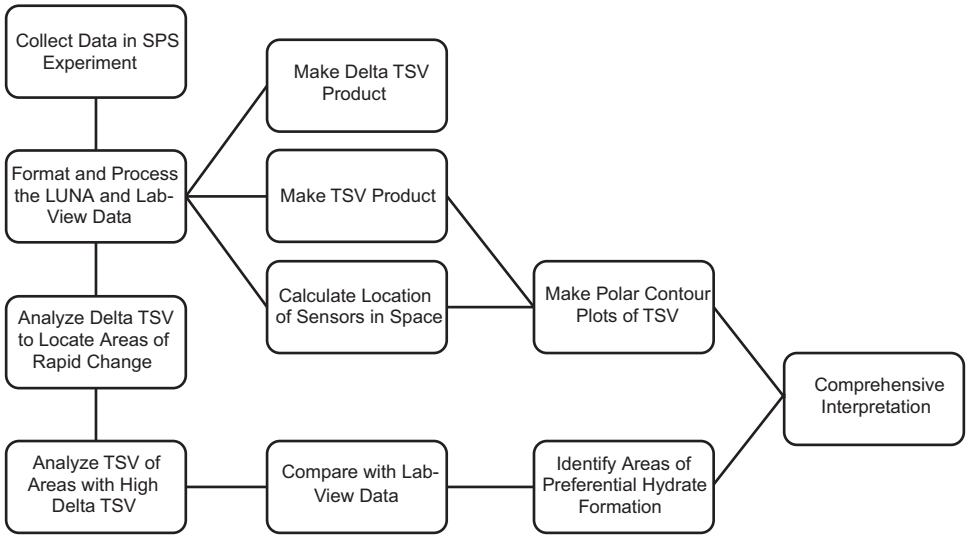

Fig. 6. Flow chart of data processing/analysis cycle. Data are analyzed through synchronous use of multiple, targeted products, each designed to identify unique properties such as TSV change or bulk pressure–temperature change.

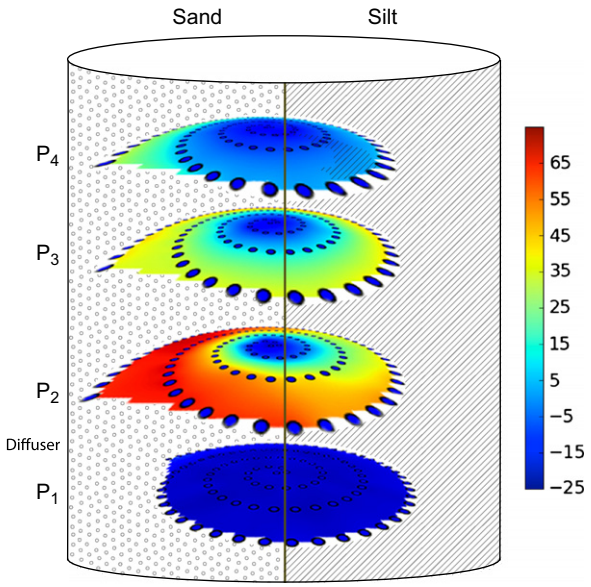

Fig. 7. Data from an experiment with a sediment column divided evenly between sand and silt along a vertical axis. Little hydrate formed on plane P_1 (below the gas diffuser). Hydrate formation on overlying planes was initially in sand (left), gradually producing hydrate in the silt (right) area. Color represents TSV. This image was obtained about 36 h after injection began. (For interpretation of the references to color in this figure legend, the reader is referred to the web version of this article.)

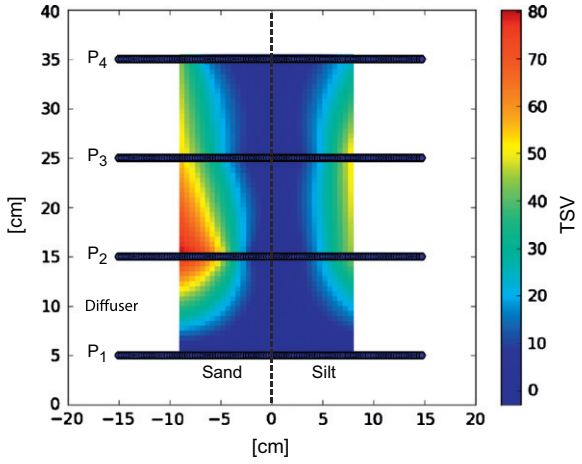

Fig. 8. A vertical slice through the column center shows more abundant hydrate in sand (left) and along vessel walls, with a color scheme similar to that of Fig. 7. Image obtained about 36 h after injection. (For interpretation of the references to color in this figure legend, the reader is referred to the web version of this article.)

boundaries between grids (edges of the warm colored zone in the sand for example) are likely due to the large vertical spacing between grids (Fig. 8). Such interpretations could be further constrained by geophysical methods, including tomography provided by seismic, electromagnetic, or electrical resistivity studies.

5. Results and discussion

The data shown in Figs. 7 and 8 are from a split column experiment in which sand was on the left side of the column, as shown, and silt was on the right side of the column. The branched diffuser assembly was placed just above the P_1 fiber grid. The split sediment column experiment showed little or no hydrate forming on the P_1 grid (below the diffuser assembly), significant formation on the P_2 grid immediately above the diffuser, and moderate formation on the top two grids (P_3, P_4). To compare all the grids on a single image, a common color scheme was chosen, which was optimized for grid 2, where the most hydrate formation was observed. Low-TSV recordings in the center of each grid are likely a strain effect from the fiber being wound tightly, as well as from the weight of the secondary pressure vessel sitting on top of the sediment column. Strain effects from the overlying mass of sand pressing down on the grids must also be considered, resulting in higher strain on the deeper grids due to the mass of overlying sediments. DSS TSV data indicate that the gas hydrate initially formed in the sand portion of the column and a small amount of hydrate formed in the silt, perhaps as a result of diffusion from the sand portion of the column. Hydrate also appears to form along the walls of the sediment column, indicating a preferential pathway for gas between the sediment and encasing plastic bucket. Ulrich et al. (2008) demonstrated that injection of non-hydrate-forming gasses results in TSV signals that are significantly different from those observed here, limited to short periods of time after injection.

6. Concluding remarks

Fiber optic sensing and data analysis methods developed here can also be applied to effectively evaluate the geological behavior of gas hydrates in complex sediment systems during drilling operations, understand the effects of environmental change on gas hydrate reservoirs, and evaluate carbon sequestration techniques. The fiber optic technology utilized here provides data from within the sediments at a resolution and spatial precision that *P–T* data cannot match. The large network of nonreactive, inexpensive, and easily deployed sensors has greatly enhanced our understanding of hydrate formation processes within mesoscale experiments. These new methods of data visualization and analysis present an opportunity to study the formation/dissociation mechanisms and pathways of gas hydrates in situ and heat flow in sediment–hydrate systems. However, there is no way to deconvolve the combined temperature–strain effect and measure true temperature or strain using the current system. In addition, absolute values for temperature or strain are not known, but relative changes can be easily determined. Interpolation of DSS planes is difficult in the current configuration because of large vertical gaps in the grid spacing. Additional fiber planes spaced closer together would be required for more reliable interpolations.

The advances in fiber optic sensing of temperature and strain have facilitated the detailed examination of mesoscale laboratory gas hydrate experiments, but also produce high-volume data sets, which are a processing and visualization challenge. The four-dimensional data can be visualized in multiple images which are then animated to avoid data shadowing, typical of 3D surface plots. By predicting the location of sensors with basic numerical techniques, the visualization can be further improved. This method of data analysis brought to light new features in the data sets and allowed a more effective comparison of DSS and *P–T* data. The DSSPlotter software is an effective tool in analysis of SPS DSS data and will aid experimenters in predicting conditions for hydrate formation and dissociation pathways in complex sediment systems.

Acknowledgments

This work was supported by the U.S. Dept. of Energy, Methane Hydrates Program through the Office of Fossil Energy field work proposal FEAB 111. We gratefully acknowledge technical support by Jonathan Alford. J. R. Leeman was supported through the Higher Education Research Experiences (HERE) program managed by the Oak Ridge Institute for Science Education (ORISE)/Oak Ridge Associated Universities (ORAU) and through the University of Oklahoma School of Geology and Geophysics. Oak Ridge National Laboratory is managed by University of Tennessee, Battelle, LLC, for the U.S. Dept. of Energy under Contract DE-AC05-00OR22725. The authors thank Bryan Chakoumakos and Ji-Won Moon for their helpful comments during ORNL internal review, two anonymous reviewers whose suggestions improved the manuscript as well, and the Computers and Geosciences Editor-in-Chief, Eric Grunsky.

Appendix A. Supplementary data

Supplementary data associated with this article can be found in the online version at doi:10.1016/j.cageo.2011.05.004.

References

Abramov, O., McEwen, A., 2004. An evaluation of interpolation methods for Mars Orbiter Laser Altimeter (MOLA) data. International Journal of Remote Sensing 25, 669–676. doi:10.1080/01431160310001599006.

Beauchamp, B., 2004. Natural gas hydrates: Myths, facts, and issues. Comptes Rendus Geoscience 336, 751–765. doi:10.1016/j.crte.2004.04.003.

Boswell, R., 2007. Resource potential of methane hydrate coming into focus. Journal of Petroleum Science and Engineering 56, 9–13.

Brewer, P.G., Peltzer, E.T., Friederich, G., Aya, I., Yamane, K., 2000. Experiments on the ocean sequestration of fossil fuel CO_2: pH measurements and hydrate formation. Marine Chemistry 72, 83–93.

Buffet, B., Archer, D., 2004. Global inventory of methane clathrate: Sensitivity to changes in the deep ocean. Earth and Planetary Science Letters 227, 158–199. doi:10.1016/j.epsl.2004.09.005.

Chatti, I., Delahaye, A., Fournaison, L., Petitet, J., 2005. Benefits and drawbacks of clathrate hydrates: A review of their areas of interest. Energy Conservation and Management 46, 1333–1343. doi:10.1016/j.enconman.2004.06.032.

Dickens, G.R., Castillo, M.M., Walker, J.C.G., 1997. A blast of gas in the latest Paleocene: Simulating first-order effects of massive dissociation of oceanic methane hydrate. Geology 25, 259–262.

Gabitto, J., Tsouris, C., 2006. Dissolution mechanisms of CO_2 hydrate droplets in deep seawaters. Energy Conversion and Management 47, 494–508.

Gao, S., House, W., Chapman, W.G., 2005. NMR/MRI study of clathrate hydrate mechanisms. Journal of Physical Chemistry 109, 19,090–19,093.

Goel, N., 2006. In situ methane hydrate dissociation with carbon dioxide sequestration: Current knowledge and issues. Journal of Petroleum Science and Engineering 51, 169–184.

Hill, K.O., Meltz, G., 1997. Fiber Bragg grating technology fundamentals and overview. Journal of Lightwave Technology 15, 1263–1276.

Jadhawar, P., Mohammadi, A.H., Yang, J., Tohidi, B., 2006. Subsurface carbon dioxide storage through clathrate hydrate formation. Advances in the Geological Storage of Carbon Dioxide, 111–126.

Jones, R.C., 1941. A new calculus for the treatment of optical systems. Journal of the Optical Society of America 31, 488–493.

Kennett, J.P., Cannariato, K.G., Hendy, I.L., Behl, R.J., 2000. Carbon isotopic evidence for methane hydrate instability during quaternary interstadials. Science 288, 128–133.

Klauda, J.B., Sandler, S.I., 2005. Global distribution of methane hydrate in ocean sediment. Energy & Fuels 19, 459–470.

Kneafsey, T.J., Tomutsa, L., Moridis, G.J., Seol, Y., Freifeld, B.M., Taylor, C.E., Gupta, A., 2007. Methane hydrate formation and dissociation in a partially saturated core-scale sand sample. Journal of Petroleum Science and Engineering 56, 108–126.

Kvenvolden, K.A., 1999. Potential effects of gas hydrate on human welfare. Proceedings of the National Academy of Sciences of the United States of America 96, 3420–3426.

Maclennan, J., Jones, S.M., 2006. Regional uplift, gas hydrate dissociation and the origins of the Paleocene–Eocene Thermal Maximum. Earth and Planetary Science Letters 245, 65–80. doi:10.1016/j.epsl.2006.01.069.

Makogon, Y.F., Holditch, S.A., Makogon, T.Y., 2007. Natural gas-hydrate—A potential energy source for the 21st century. Journal of Petroleum Science and Engineering 56, 14–31.

Max, M.D., Dillon, W.P., Nishimura, C., Hurdle, B.G., 1999. Sea-floor methane blowout and global firestorm at the K–T boundary. Geo-Marine Letters 18, 285–291.

Mienert, J., Vanneste, M., Bünz, S., Andreassen, K., Haflidason, H., Sejrup, H.P., 2005. Ocean warming and gas hydrate stability on the mid-Norwegian margin at the Storegga Slide. Marine and Petroleum Geology 22, 233–244.

Moridis, G.J., Collett, T.S., Boswell, R., Kurihara, M., Reagan, M.T., Koh, C., Sloan, E.D., 2009. Toward production from gas hydrates: Current status, assessment of resources, and simulation-based evaluation of technology and potential. SPE Reservoir Evaluation & Engineering 12 (5), 745–771.

Padden, M., Weissert, H., Rafelis, M., 2001. Evidence for Late Jurassic release of methane from gas hydrate. Geology 29, 223–226.

Phelps, T.J., Peters, D.J., Marshall, S.L., West, O.R., Liang, L., Blencoe, J.G., Alexiades, V., Jacobs, G.K., Naney, M.Y., Heck, J.L., 2001. A new experimental facility for investigating the formation and properties of gas hydrates under simulated seafloor conditions. Review of Scientific Instruments 72, 1514–1521.

Rawn, C.J., Leeman, J.R., Ulrich, S.M., Alford, J.E., Phelps, T.J., Madden, M.E., 2011. Fiber optic sensing technology for detecting gas hydrate formation and decomposition. Review of Scientific Instruments 82, 024501. doi:10.1063/1.3514983.

Sibson, R., 1981. A brief description of natural neighbor interpolation. In: Interpreting Multivariate Data, John Wiley & Sons, New York.

Sloan, D.E., 1998. Clathrate Hydrates of Natural Gasses, second ed. Marcel Dekker, New York, NY, 705 pp.

Thompson, H., Soper, A.K., Buchanan, P., Aldiwan, N., Creek, J.L., Koh, C.A., 2006. Methane hydrate formation and decomposition: Structural studies via neutron diffraction and empirical potential structure refinement. Journal of Chemical Physics 124 (16), 164508.

Ulrich, S.M., Elwood-Madden, M.E., Rawn, C.J., Szymcek, P., Phelps, T.J., 2008. Application of fiber optic temperature and strain sensing technology to gas hydrates. In: Proceedings of the 6th International Conference on Gas Hydrates, Vancouver, Canada.

Waite, W.F., Winters, W.J., Mason, D.H., 2004. Methane hydrate formation in partially water-saturated Ottawa sand. American Mineralogist 89, 1202–1207.

Walsh, M.R., Hancock, S.H., Wilson, S.J., Patil, S.L., Moridis, G.J., Boswell, R., Collett, T.S., Koh, C.A., Sloan, E.D., 2009. Preliminary report on the commercial viability of gas production from natural gas hydrates. Energy Economics 31, 815–823.

Weissert, H., Erba, E., 2004. Volcanism, CO2 and palaeoclimate: a Late Jurassic–Early Cretaceous carbon and oxygen isotope record. Journal of the Geological Society 161, 695–702.